PCCP

Accepted Manuscript

ROYAL SOCIETY OF CHEMISTRY

www.rsc.org/pccp

Physical Chemistry Chemical Physics RSCPublishing

ARTICLE

Tuning the Optical, Electrical and Magnetic Properties of $Ba_{0.5}Sr_{0.5}Ti_xM_{1-x}O_3$ (BST) Nanopowders

Cite this: DOI: 10.1039/x0xx00000x

Received 00th January 2012,
Accepted 00th January 2012

DOI: 10.1039/x0xx00000x

www.rsc.org/

Ali Omar Turky,[*a,c] Mohamed Mohamed Rashad,[a] Abd El-Hakim Taha Kandil,[b] and Mikhael Bechelany[c]

Metal doped barium strontium titanate (BST; $Ba_{0.5}Sr_{0.5}Ti_xM_{1-x}O_3$) nanopowders have been successfully synthesized through the oxalate precursor route based on low cost starting materials. The effect of metal ion substitution namely; Fe^{3+}, Mn^{2+}, Co^{2+} and Y^{3+} on the crystal structure, microstructure and optical, electrical, dielectric and magnetic properties of BST was studied. The results revealed that well crystalline single cubic BST phase was formed for pure and Mn^{2+}, Co^{2+} and Y^{3+} ion substituted BST samples whereas tetragonal BST structure was obtained for Fe^{3+} substituted BST sample at annealing temperature 1000°C for 2h. Furthermore, addition of the metal ions was found to decrease the crystallite size and unit cell volume of the produced BST phase. The microstructure of the produced pure BST phase was metal ion dependent. Most of BST particles were appeared as cubic like structure. The transparency of BST was found to increase with metal substitution. Meanwhile, the band gap energy was increased from 3.4 eV for pure BST to 3.8, 4.1, 4.2 and 4.3 eV as the result of substitution by Fe^{3+}, Mn^{2+} and Co^{2+} and Y^{3+} ions, respectively. The DC resistivity was metal ion dependent. The highest DC resistivity (ρ = 66.60 x 10^5 Ω. cm**)** was accomplished with Mn^{2+} ion. Moreover, the addition of metals ion was decreased the dielectric properties expected Mn^{2+} ion and increased the magnetic properties.

A. Introduction

Generally, ABO_3 is a perovskite structure which their corner structure shares in BO6 octahedron. The A-site cations occupy in 12-fold coordination site that is in the middle of polyhedral structure. The A- and B-sites generally are a rare earth and a transition metal cation, respectively. Among then, $(Ba_{0.5}Sr_{0.5})TiO_3$ powders (BST) is one of the well known attractive perovskite materials with unique properties *i.e.* high dielectric constant, good chemical and thermal stability, low dielectric losses and low current leakage. Due to such desirable properties, BST ceramics have been widely used in various applications such as dynamic random, access memory, ceramic capacitors, pyroelectric sensors, infrared detectors, chemical sensor, biosensor, microwave devices and optoelectronic applications.[1-5] Furthermore, it is widely used in microelectronic mechanical system (MSMS) applications due to the ferroelectric characteristics.[6-8]

The properties of BST can easily be modified by addition of materials that form solid solutions in the perovskite structure. The first additive used are the isovalent ones, i.e. Pb^{2+}, Sr^{2+}, Ti^{4+}, Ca^{2+} and Zr^{4+} which are replaced partially on both A and B site with the same chemical valence and similar ionic radii as those of the replaced ions. The major effect of such isovalent additives is lowering of the Curie temperature and dielectric loss, giving enhanced permittivity (higher dielectric constant).[9-10] Various wet-chemical methods have been reported for the preparation of BST powders including co-precipitation, organic compound method, sol gel process, hydrothermal method.[11-18] Among these methods, there are two main ways for the generation of BST powders. One is the direct synthesis of BST powders under the hydrothermal conditions (dissolution and re-crystallization) by using the conventional materials.[19] The second important way for the preparation of BST powders is via the precipitation of a molecular precursor namely, barium strontium titanyl oxalate (BSTO), pyrolysis of which at an elevated temperature to produce BST powders.[20] It is well known that some dopants are able to modify and improve the properties of dielectric materials, including BST. According to the previous investigations,[21-22] the optical and electrical properties (dielectric constant, dielectric loss) of BST powders are affected by the synthesis processes, microstructure, and the type of dopant. Particularly, The acceptor substitution with lower positive valence ions replace metal ions with a higher positive valence oxygen vacancies are created in the lattice occupy the B site in the ABO_3 perovskite structure is acceptor substitution. Different dopants such as Fe^{2+}, Fe^{3+}, Co^{2+}, Co^{3+}, Mn^{2+}, Mn^{3+}, Ni^{2+}, Mg^{2+}, Al^{3+}, Ga^{3+}, In^{3+}, Cr^{3+} and Sc^{3+} are used.[23-25] The advantages of acceptor substitution are that they lead to lower dielectric constant, lower dielectric loss, higher coercive field, lower resistivity and inhibited grain growth[23-

[25]. Furthermore, the donor additives by Bi^{3+} and rare earth elements occupy A-site to increase dielectric constant and the dielectric loss and lowering the Curie temperature[26]. Nevertheless, although the positive effect of doping for the BST is rather clear, the investigations made before involved only few types of dopants. Therefore, the previous work does not enough provide information to improve the characteristics of the BST powders for the applications in tunable microwave and electro-optics devices. Herein, barium strontium titanate was successfully synthesized through oxalate precursor method based on low cost starting materials using titanium oxide as the source of Ti^{4+} ion instead of expensive Ti alkoxides materials. Meanwhile, effects of Fe^{3+}, Mn^{2+}, Co^{2+}, and Y^{3+} substituted BST on the crystal structure, crystallite size, microstructure, optical properties, electrical resistivity and magnetic properties were also investigated.

B. Materials and methods

1. Materials

Pure and doped barium strontium titanate nanopowders were synthesized through oxalate precursor method according to the empirical formula $(Ba_{0.5}Sr_{0.5})Ti_{0.8}M_{0.2}O_3$ (M=Fe^{3+},Mn^{2+}, Co^{2+}) in the case of acceptor dopants and the empirical formula $(Ba_{0.5}Sr_{0.5})_nY_{1-n}TiO_3$ (n=Y^{3+}) in case of donor dopants. All the chemicals used in this study such as barium nitrate $Ba(NO_3)_2$, $Sr(NO_3)_2$ (98.6%, BDH Chemical Ltd), Titanium dioxide TiO_2 (Fluka> 99.8% purity), $Fe(NO_3).9H_2O$ (prolabonorma pour analysis made from France), $Mn(NO_3)_2$ (BDH laboratory suppliers made in England), $CoCl_2.6H_2O$ (Acros Organics USA), $Y(NO_3)_3.6H_2O$ (Sigma Aldrich), oxalic acid as source of organic acid (organic 90%, El Nasr Chemical Co.) were of analytical grade. Deionized water was used in the whole work.

2. Fabrication Procedures

Barium strontium titanate (BST) nanopowders were prepared using aqueous solutions of barium nitrate $Ba(NO_3)_2$ and $Sr(NO_3)_2$ with molar ratios of 0.5 Ba^{2+} and 0.5 Sr^{2+}. The metal doping molar ratios are 0.2 for all samples. A certain amount of oxalic acid related to stoichiometric ratios of (Ba^{2+}, Sr^{2+}) and Ti^{+2} was added to the solution. The solution was stirred and evaporated at 80°C till a clear, viscous gel was obtained, and then dried at 110 °C for 24 h. The dry precursors were heated at a rate of 10 °C/min in static air at maximum temperatures of 1000°C during 2 h. The produced barium strontium titanate was evaluated by means of several characterizing tools.

3. Chemical and physical characterization

X-ray powder diffraction (XRD) was carried out on a model Bruker AXS diffractometer (D8-ADVANCE Germany) with Cu Kα (λ = 1.54056 Å) radiation, operating at 40 kV and 40 mA. The diffraction data were recorded for 2θ values between 10° and 80° and the scanning rate was 3 min^{-1} (0.02°/0.4 s). Scanning electron microscopy was investigated by a SEM (JEOL-JSM-5410 Japan). The UV-vis absorption spectrum was measured by UV-VIS-NIR-scanning spectrophotometer (jasco-V-570 spectrophotometer Japan) using a 1 cm path length quartz cell. The spectrum obtained for the barium strontium titanate nanostructures which ultrasonicated in deionized water to yield homogeneous dispersion pure distilled water solution used as a blank. An electrometer and DC power supply (Agilent-4339B, USA) were used for electrical resistivity measurement for the experimental studies. The DC resistivity is given by

$$\rho = \frac{RA}{L} \qquad \text{Equation (1)}$$

Where R is the resistance ,A is the area of the disc and L is the thickness of the disc. The method used for the DC resistivity measurement is two contact methods. A constant DC voltage (V) of about 1.5 V was applied from a battery across the sample. Dielectric properties were measured using a network impedance analyzer (Agilent-E4991A, USA) that is responsible for the generation and reception of a signal in the frequency range of 1 MHz to 3 GHz. In fact, the full dielectric constant contains a real part and a image part:

$$\varepsilon = \varepsilon' + j\varepsilon'' \qquad \text{Equation (2)}$$

The loss tangent tanδ is proportional to the dielectric loss, it means the EM energy is converted to heat energy because of the dielectric are lost. The dissipation loss means the radiation of energy when EM is propagating, because the microstrip line is an open structure.

$$Tan\delta = \frac{\varepsilon''}{\varepsilon'} \qquad \text{Equation (3)}$$

The loss tangent is defined as well by the tangent of the difference of the phase angle between capacitor voltage and capacitor current with respect to the theoretical 90 degree value anticipated, this difference being caused by the dielectric losses within the capacitor. The value δ (Greek letter delta) is also known as the loss angle.

$$Tan\delta = DF = \frac{1}{Q} = \frac{ESR}{Xc} \qquad \text{Equation (4)}$$

Where δ = loss angle (Greek letter delta), DF = Dissipation factor
Q = quality factor, ESR = equivalent series resistance and
Xc = reactance of the capacitor in ohms.

C. Results and discussion

1. Synthesis metal doped BST nanopowders

Figure 1 shows the XRD patterns of $Ba_{0.5}Sr_{0.5}Ti_{1-x}M_xO_3$ (where M= Fe, Co, Mn, and Y) with metal concentration equal to 0.2 M synthesized through oxalate precursor method annealed at 1000°C for 2h. In the case of Fe^{+3} doping, it is clear that no impurity iron oxide phase was matched in the $Ba_{0.5}Sr_{0.5}Ti_{1-x}Fe_xO_3$ (BSTF) patterns. Meanwhile, well defined tetragonal prevoskite phase can be deduced, with higher intensity without any detectable secondary cubic phase in BSTF patterns. The XRD peak at 2θ = 46° shows splitting for BSTF which indicates a tetragonal structure. It is evident that reflection peaks at 2Θ =22.05, 31.6, 39.2, 45.9, 50.9, 56.2, 66.8, 71.3 and 76.5° belonging to (100), (110), (111), (002), (210), (211), (220), (212), (310) and (311) diffraction planes of tetragonal phase were ascribed, respectively. Furthermore, no extra lines corresponding to the residual carbonates phases, such as $BaCO_3$, $SrCO_3$ and $(Ba,Sr)CO_3$ were observed in Figure 1 resulting from the reaction of BaO with atmospheric CO_2 and the burn-out of organic materials or as a result of incomplete calcination. Otherwise, the XRD profile of $Ba_{0.5}Sr_{0.5}Ti_{1-X}Co_XO_3$ (BSTC) powders substituted with 0.2 molar ratio of Co^{2+} ion are evinced in Figure 1. One can be note that cubic perovskite structure affined to paraelectric phase BST was exhibited. Besides, Co^{2+} ion doping had resulted in a very small increase of the in-plane (*a*-plane) lattice parameter whereas the variations in the out-of-plane (*c*-plane) lattice parameter are negligible (Table 1).[27-29]

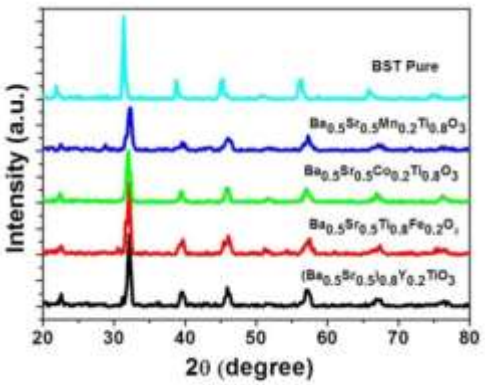

Figure 1. XRD patterns of produced pure BST and BST with different metal ions substitution (Fe^{3+}, Mn^{2+}, $Co^{2+}$and Y^{3+}) annealed at 1000°C for 2 h

Furthermore, the crystal structure for Mn^{2+} ion substituted $Ba_{0.5}Sr_{0.5}Ti_{1-x}Mn_xO_3$ (BSTM) elucidated that the diffraction planes (100), (110), (111), (200), (210) and (211) related to cubic BST perovskite phase were confirmed. It is well known that the Mn^{2+} ionic radius (0.8 Å) was smaller than those of Ba^{2+}(1.35 Å) and Sr^{2+} (1.13 Å) ions and it was larger than that of Ti^{4+}(0.61Å) ion. Hence, increasing the lattice parameter (*a*) of BSTM sample demonstrated that Ti^{4+} ion was replaced by Mn^{2+} at the B-sites (Table 1).[30-32]

Table 1. The structure parameters of pure and metal substituted BST samples

Metal ions doped	Crystallite size (nm)	Lattice parameter (Å)		Unit cell volume ($Å^3$)
		a	*c*	
BST	36.4	3.945	-	61.40
BSTF	33.8	3.889	3.920	59.29
BSTC	31.1	3.939	-	61.12
BSTM	27.2	3.889	-	58.82
BSTY	28.6	3.917	-	60.09

Of note, the diffraction pattern of Y^{3+} ion substituted $(Ba\text{-}Sr)_{1-n}Y_nTi_1O_3$ (BSTY) where n=0.2 was assigned to cubic perovskite BST. Indeed, the diffraction planes (100), (110), (200) and (211) were referred to cubic BST structure. There are no reflections belonging to Y_2O_3 phase. It is worth mentioning in this context that Y^{3+} ion can mainly substitute A site (Ba^{2+}, Sr^{2+}) ions and B site (Ti^{4+}) ion when the concentration was increased from 0.1 to 0.2 mol %. , leading to the shifting of the (110) peak to a higher angle, *i.e.* a decrease in lattice spacing (Table 1). Furthermore, the increasing of Y^{3+} concentration from 1.0 to 1.2 mol %, led to the perovskite lattice to slightly expand. The results are imputed to the radius of Y^{3+} (0.93 Å) near to those of Sr^{2+} and Ba^{2+} ions. Besides, it is known that Ti^{4+} in 6 coordinates are 0.161, 0.144 and 0.061 nm, whereas Y^{3+} in 12 and 6 coordinates are 0.106 and 0.086 nm, respectively. Therefore, in terms of size, Y^{3+} ion can occupy either the A or B site in BST solid solution, and the crystal lattice parameter of the samples will be changed. [33-34]

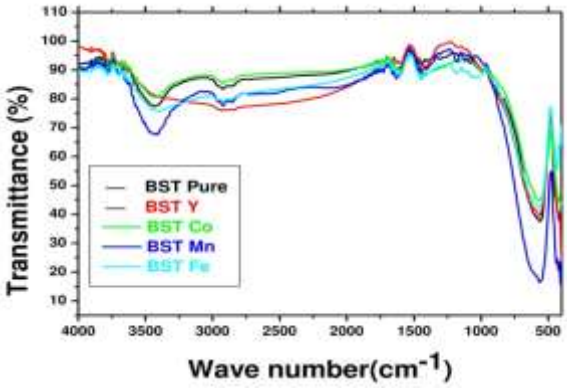

Figure 2. FT-IR spectra of BST doped with acceptor and donor metals at oxalic acid molar ratio of 1 and annealed at 1000°C for 2 h

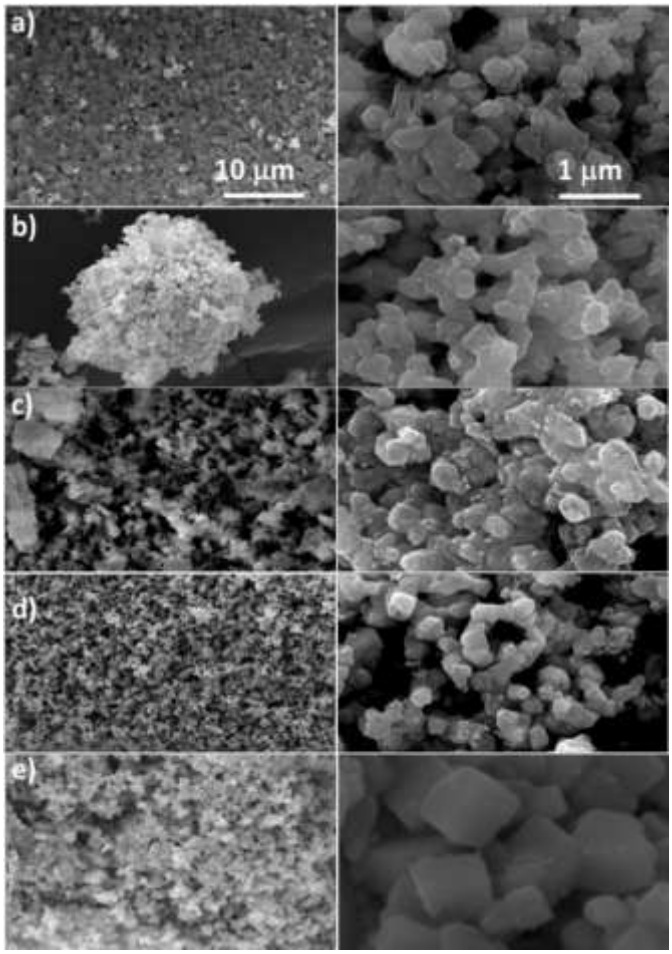

Figure 3. FE-SEM images of the produced pure BST and metal doped BST powders (a) Fe^{+3}, (b) Co^{+2}, (c) Mn^{+2}, (d) Y^{+3} and (e) pure BST

Figure 2 depicts the FT-IR spectrum of the metal doped BST powders annealed at 1000°C for 2h. The main bands characteristic of the oxygen–metal bond were assigned in the region 450–640 cm^{-1}. Due to the absence of a C=O vibration around 1450 cm^{-1}, it can be addressed that the powders were carbonate free. This result is satisfactory from a technological point of view since the electrical properties are dependent on the quality of the raw powders used to sinter the ceramic.[35] Besides, a vibration band associated to the deformation of O-H bonds near 1680 cm^{-1} was observed due to the water adsorbed at the powder surface when the sample was in contact with the environment. Additionally, Furthermore, the bands corresponding to 3400 cm^{-1} and 1420 cm^{-1} were represented the stretching and bending vibrations of H–O–H and indicated the presence of free or absorbed water the absorption bands whereas the band at 570 cm^{-1} corresponding to Ti-O stretching vibrations, was evidenced in the spectrum.[36-37]

Fig.3 presents scanning electron microscope images which reveal the morphology and the size of pure, 0.2 molar ratio of Fe^{3+}, Co^{2+}, Mn^{2+} and Y^{3+} substituted BST samples, respectively. It is clear that the grain size of BST particles was decreased with metal substitution in compared with pure BST sample. Indeed, the grain size of the powder was ranged from 50 to 200 nm. Otherwise, the grain size of Y^{+3} doped BST sample showed the lowest grain size compared with the other substituted metals. Meanwhile, most of the formed BST samples were in uniform microstructure with highly agglomeration. Moreover, one can note that the all metals substituted BST particles were exhibited cubic-like structure expected Fe^{3+} substituted BST with unclear microstructure. Table 2 represents EDX analysis of pure and metal doped BST samples. It can be seen that chemical analysis of pure and metal doped BST samples were consistent with the structure. The peaks positions of Fe^{2+}, Co^{2+}, Mn^{2+} and Y^{3+} were detected with the peaks of Ba^{2+}, Sr^{2+}, Ti^{4+} and O^{2-}. The atomic weight, % of the formed compounds was related to the substituted molar ratio of the doped metal ion.[38]

Table 2. Energy-dispersive X-ray spectroscopy (EDX) analysis of metal doped BST prepared by oxalic acid precursor method annealed at 1000°C for 2h

	Element weight %							
Sample ID	**Ba**	**Sr**	**Ti**	**O**	**Fe**	**Mn**	**Co**	**Y**
BST	21.66	30.85	9.44	38.05				
BSTF	30.94	17.09	13.71	32.34	5.92			
BSTM	22.41	25.67	16.01	30.62		5.29		
BSTC	32.00	17.09	15.69	30.05			5.17	
BSTY	25.67	20.41	21.00	28.48				4.44

2. Optical properties

The optical constants of BST nanopowders are highly influenced by the structure, the composition and the fabrication method. To determine the optical parameters, the optical transmittance spectrums of the metal doped BST samples have been recorded in the wavelength range 200–800 nm as shown in Figure 4. The transmittance of metal doped BST samples was higher than the undoped BST sample. The transmittance percentage was accomplished ~ 88% with Y^{3+} substituted BST sample whereas the transmittance of pure BST was exceeded only 45%. In the optical absorption-related experiments, it is well known that the fundamental absorption refers to the valence band (VB)-to-conduction band (CB) transition, from which the band gap energy (Eg) can be estimated by assuming a direct transition between the bands. From UV-Vis transmittance spectrum, the band-gap of BST nanopowders can be calculated with the following equations:

$$I = I_o x e^{-\alpha t} \quad \text{(Equation 5)}$$

$$(\alpha h\nu)^n = A(h\nu - E_g) \quad \text{(Equation 6)}$$

In equation 5, I is the intensity of the transmitted light, I_0 is the intensity of the incident light, t is the thickness of covet and α is the absorption coefficient. In equation 6, hν represents the photon energy, Eg is the band-gap energy and A is a constant while n depends on the nature of the band-gap (n = 1/3 for indirect forbidden transition, n = 1/2 for indirect allowed transition, n = 2/3 for direct forbidden transition, and n = 2 for direct allowed transition). The intercept of a $(\alpha h\nu)^n$ versus hν plot determines the band-gap of the materials.[36, 39]

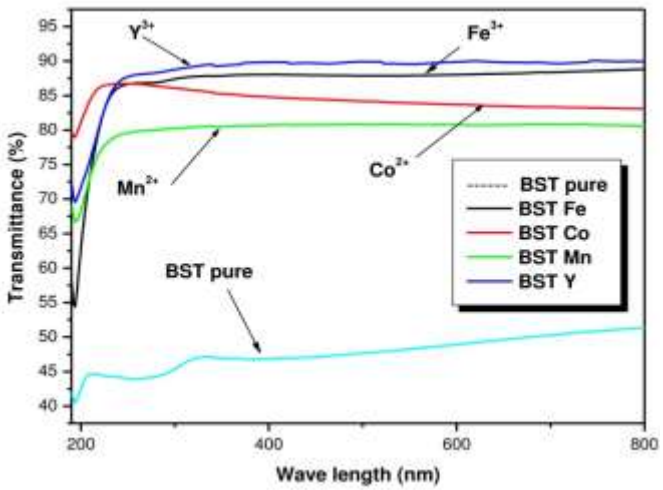

Figure 4. UV–visible transmittance spectrum (T %) of metal doped BST nanopowders synthesized using oxalate precursor route annealed at 1000°C for 2h

Table 3. The value of band gap energy for pure and metal doped BST samples

Sample ID	Band gap energy value (eV)
BST	3.4
BSTF	3.8
BSTC	4.1
BSTM	4.2
BSTY	4.3

Table 3 deduced the band gap energy values for pure and metal doped BST. It can be seen that the band gap energy was increased with addition of metal concentration. Hence, the band gap energy was increased from 3.4 eV for pure BST to 3.8, 4.1, 4.2 and 4.3 eV for BSTF, BSTC, BSTM and BSTY samples, respectively. This elucidated that doping metals caused the compressive stress relaxation in the BST samples. Such peak shift is usually compensated by the grain size effect as the results of a combination of quantum-size effect in small grains, existence of amorphous phase, as well as biaxial stress in the BST samples.[40] Cavalcante *et al* [41] indicated that the increasing in the band energy gap with doped metals can be related to the degree of structural order–disorder in the lattice. Therefore, the increase of structural organization in the BST films leads to a reduction of the intermediary energy levels and consequently increases the Eg values. These intermediary energy levels are localized below the conduction band. Wang *et al* [42] showed that the variation of the band gap energy is mostly likely predominantly due to the change in electronic structure associated with the larger lattice parameter and perhaps some variations in

atomic co-ordination. The packing density, the oxygen deficiency and the grain size should play an important role on the optical properties. The results, *e. g.* the dependence of the optical band-gap energies on the grain size, were discussed in details by several authors. Thielsch *et al* [43] analyzed the laser-deposited BST thin films on MgO (001), who found that films with smaller crystallite exhibited larger band-gap energies than those with larger grains. All the above results show that the optical properties of $Ba_{0.5}Sr_{0.5}TiO_3$ powders are easily controlled, which indicates BST samples are a promising candidate for electro-optic applications.[41]

3. DC Resistivity

Table 4 lists the change of DC resistivity with different metal doped BST. The results evinced that the DC resistivity was decreased with metal doped BST expected Mn^{2+} ion. It is clear that the lowest DC resistivity (78.93 x $10^3\Omega$.cm) was achieved with 0.2 Fe^{3+} ratios due to the phase transformation of BST from cubic to tetragonal structure. However, the DC resistivity was also decreased with Co^{2+} and Y^{3+} substituted BST samples compared with pure BST. The results are attributed to the increasing of the pores and the decreasing of the grain size and the packing density of the formed metal doped BST samples. The highest DC resistivity was reached for Mn^{2+} ion substituted BST sample. The Mn incorporated in the oxygen octahedron of the BST unit cell was in a more centered position than Ti. Thus, the increasing of the resistivity of Mn doped BST sample was related to mismatch of the oxidation state between Mn^{2+}/Mn^{3+} by replacing Ti^{4+} ion. Because Mn^{2+} and Mn^{3+} are more reducible than the Ti, the electrons were trapped at these sites. Consequently, the hopping motion of the trapped electrons from one Mn site to another was almost prohibited. Furthermore, the increasing of electrical resistivity was most likely due to the combination of Mn-O-Mn network strain and scattering by the random potential introduced by Mn substitution[44].

Table 4. Variation of the valuable of DC resistivity with different metal doped BST

Sample ID	ρ (Ω.cm)
BST	$54.10x10^5$
BSTF	$78.93x10^3$
BSTM	$66.60x10^5$
BSTC	$28.71x10^4$
BSTY	$21.10x10^4$

4. Dielectric properties

Table 5. Summary of real and imaginary permittivity parts measurements of BST with different compositions at gigahertz frequency and room temperature

	Dielectric parameters		
BST composition	**ε'**	**ε''**	**Tan δ**
BST	144.5	245.38	0.588
BSTF	65.6	115.78	0.566
BSTC	68.8	193.33	0.355
BSTM	152	281.44	0.540
BSTY	114	195.06	0.584

Figure 5 depicts the variation in the real and imaginary permittivity parts and the dielectric loss (loss tangent) of the metal doping $Ba_{0.5}Sr_{0.5}M_xTi_{1-x}O_3$ (M = Fe^{3+}, Mn^{2+}, Co^{2+}) where (X=0.2) and donor doping $(Ba_{0.5}Sr_{0.5})_{1-n}Y_nTiO_3$ as the function of the frequency at room temperature from 1 MHz to 3 GHz. It was noticeable that the specimens were decreased with the metal addition expected Mn^{2+}. For the acceptor doping, this phenomenon was due to the occupation of Ti^{4+} sites by these ions (Fe^{3+}, Mn^{2+}, and Co^{2+}). The substitution might produce oxygen vacancies, which lead to a 'break' of the cooperative vibration of Ti–O chains and bring about a decrease in the c/a ratio. This 'break' is responsible for the lower Tc of the doped BST [41, 43] at room temperature. The loss tangent of all the doped samples was increased compared with that of the pure BST when measured at low frequency (1 MHz), especially the Y^{+3} doped sample, as shown in Table 5. This may be attributed to the Y^{3+} occupation of the Ba^{2+}/Sr^{2+} site which probably increased the conductivity of the specimen. Because the donor impurity center bears an effective positive charge relative to the ideal lattice of the host oxide, and required charge compensation by a species having an effective negative charge, e.g., a cation vacancy or an electron, so this increases the free carriers of the specimen and increases the loss tangent.[43, 45] Furthermore, it is clear that the dielectric loss (loss tangent) of these specimens was increased much compared to that observed. This is probably as the result of the dielectric relaxation and phonon interaction with defect in these specimens. The loss tangent data at 1 GHz between the doped and the undoped samples was not varied much and the loss tangent of the metals doped decreases slightly than the pure BST.[34]

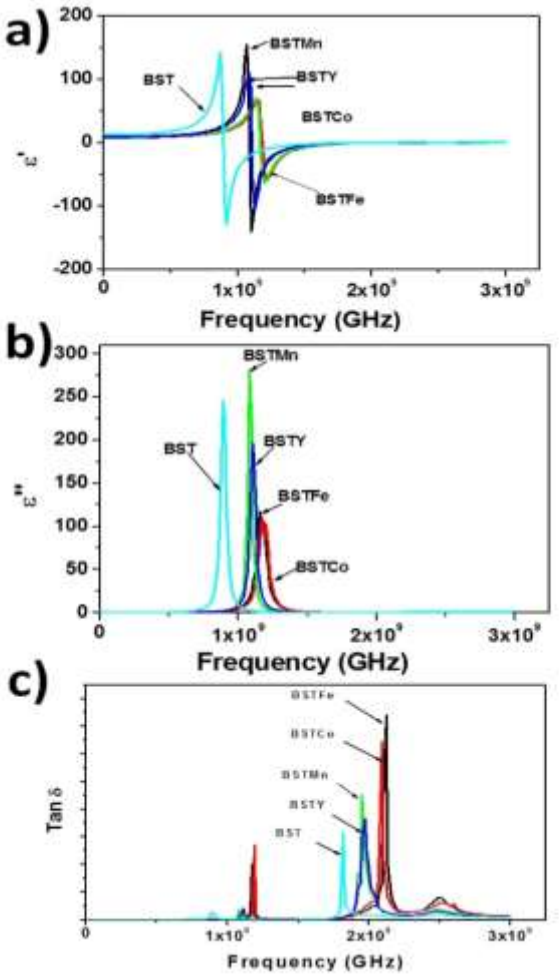

Figure 5. The relation between the (a) real part of permittivity (b) imaginary part permittivity. (c) The loss factor of tan δ with frequency for BST samples pure and metal ion substituted prepared by oxalic acid precursor route.

5. Magnetic properties

Figure 6 depicts magnetic hysteresis loops of pure and metal doped $Ba_{0.5}Sr_{0.5}Ti_xM_{1-x}O_3$ (BSTM) (where x = 0.0 and 0.2). The magnetic properties of materials are usually characterized by a hysteresis loop, which gives the behavior of materials when excited by an external magnetic field. From the graphs, it is noted that when BST doped with other metal exhibit a typical magnetic hysteresis at room temperature, indicating that the BST materials are magnetically ordered. The magnetization measurements reveal that all metals atom are dissolved in $Ba_{0.5}Sr_{0.5}TiO_3$ host lattice with no impurities such as metallic iron and iron oxides existing in the samples. It can be seen that the Fe^{3+} substituted BST exhibits weak ferrimagnetic characteristics with high coercive force extending 3636 Oe and saturation magnetization (*Ms*= 0.284 emu/g) which imputed to the Fe^{3+} atom occupying the B site. Furthermore, the improved in magnetic properties were related to the decreasing in the grain size by Fe substitution. Otherwise, the BSTC (*Ms*=0.05 emu/g) and BSTM (*Ms*=0.0435 emu/g) have weak ferromagnetic characteristics which attributed to the magnetic moments come from Co^{2+} and Mn^{2+} distributed over the pentahedral and octahedral site of Ti^{4+} ion.[45] It is worth mentioning in this context to the fact that that magnetism in ceramic oxides nanopowders arises from vacancies. From Table 6, the oxygen vacancies for BSTF, BSTC and BSTM was increased by substitution with different transition elements, respectively, as a result of different ionic radius, where Fe^{3+}, Co^{2+} and Mn^{2+} ions mainly acts as an acceptor to replace Ti in the B-site, leading to the further ionization of Fe^{3+}, Co^{2+} and Mn^{2+} ions and the appearance of lattice defects and vacancies, which are favorable for increasing the magnetization in ceramics materials[46]. Therefore, the super exchange interactions between metal ions in different occupational sites with oxygen vacancies are expected to produce the observed ferromagnetism. However, the antiferromagnetic characteristics of A-site Y^{3+} doping BST may be related to the oxygen deficiency induced by change the valence from Ti^{4+} to Ti^{3+} and the formed the charge imbalance in the lattice.[46]

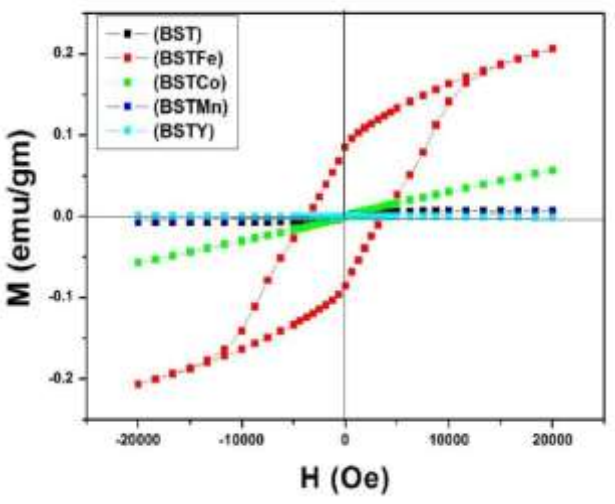

Figure 6. Room-temperature M–H hysteresis loops of the pure and metal ion doped BST samples synthesized via oxalate precursor route and annealed at 1000°C for 2 h

Table 6. The magnetic properties of pure and metal ions substituted BST synthesized via oxalate precursor route annealed at 1000°C for 2h

	Magnetic parameters			
Composition	***Ms* (emu/g)**	***Mr* (emu/g)**	***Hc* (Oe)**	**Mass (gm)**
BST	0.007	0.0004	83.07	0.096
BSTF	0.284	0.1178	3636.0	0.095
BSTC	0.057	0.0003	77.04	0.093
BSTM	0.044	0.0011	233.5	0.098
BSTY	0.007	0.0022	4147.0	0.093

Conclusions

In summary, the acceptor (Fe^{3+},Mn^{2+},Co^{2+}) and donor Y^{3+} doped $Ba_{0.5}Sr_{0.5}TiO_3$ nanopowders have been synthesized using oxalate precursor method based on low cost starting materials. The obtained materials were fully characterized. The results demonstrated that all the substituted metals have a strong effect on the grain size and the optical, electrical, dielectric and magnetic properties of the formed BST samples. XRD patterns revealed that well crystalline single cubic BST phase was formed for pure and Mn^{2+}, Co^{2+} and Y^{3+} ion substituted BST samples whereas tetragonal BST structure was obtained for Fe^{3+} substituted BST sample at annealing temperature 1000°C for 2h. FESEM images showed that the studied samples exhibited regular cubic like structure expected Fe^{3+} doped BST sample which displayed unclear microstructure. A highly transparent Y doped BST sample with a transmittance of ~ 88% in the visible region was evinced. The band gap energy was increased with metal substitution. Consequently, the band gap energy was increased from 3.4 eV for pure BST to 3.8, 4.1, 4.2 and 4.3 eV as the result of substitution by Fe^{3+}, Mn^{2+} and Co^{2+} and Y^{3+} ions, respectively. Otherwise, the resistivity was reached 66.60 x 10^5 Ω.cm for the Mn doped BST sample. The variation in the relative real and imaginary parts of permittivity and the loss tangent as a function of the frequency at room temperature indicated the decreasing with doped metals expected Mn2+ ion compared with pure BST. Moreover, it can be seen that the Fe^{3+} substituted BST exhibits weak ferrimagnetic characteristics with high coercive force extending 3.6 kOe and saturation magnetization (*Ms*= 0.284 emu/g) which imputed to the Fe^{3+} atom occupying the B site. However, the Co^{2+} and Mn^{2+} ion substituted BST have weak ferromagnetic characteristics which attributed to the magnetic moments come from Co^{2+} and Mn^{2+} distributed over the pentahedral and octahedral site of Ti^{4+} ion.

Notes and references

This work was partially supported by the French Government through a fellowship granted by the French Embassy in Egypt (Institut Français d'Egypt).

[a] Central Metallurgical Research and Development Institute, P.O. Box: 87 Helwan, Cairo, Egypt

[b] Faculty of Science, Helwan University, Helwan, Egypt

[c] Institut Européen des Membranes, UMR 5635 ENSCM UM2 CNRS, Université Montpellier 2, Place Eugène Bataillon, 34095 Montpellier, France

* Corresponding author: ali_omar155@yahoo.com

1. K. Su, N. Nuraje and N.-L. Yang, *Langmuir*, 2007, **23**, 11369-11372.
2. S. Mornet, C. Elissalde, V. Hornebecq, O. Bidault, E. Duguet, A. Brisson and M. Maglione, *Chemistry of Materials*, 2005, **17**, 4530-4536.

3. Xie, Dong, Chen and Lin, *Industrial & Engineering Chemistry Research*, 2005, **44**, 811-815.
4. J. Xu, J. Zhai and X. Yao, *Crystal Growth & Design*, 2006, **6**, 2197-2199.
5. Y.-S. Ham and J.-H. Koh, *Solid State Sciences*, 2013, **16**, 53-56.
6. T. Tubchareon, S. Soisuwan, S. Ratanathammaphan and P. Praserthdam, *Journal of Luminescence*, 2013, **142**, 75-80.
7. P. K. Sharma, V. V. Varadan and V. K. Varadan, *Chemistry of Materials*, 2000, **12**, 2590-2596.
8. J. A. Dawson, D. C. Sinclair, J. H. Harding and C. L. Freeman, *Chemistry of Materials*, 2014.
9. K. Bethe and F. Welz, *Materials Research Bulletin*, 1971, **6**, 209-217.
10. S. García, R. Font, J. Portelles, R. J. Quiñones, J. Heiras and J. M. Siqueiros, *J Electroceram*, 2001, **6**, 101-108.
11. G. B. Alers, R. M. Fleming, Y. H. Wong, B. Dennis, A. Pinczuk, G. Redinbo, R. Urdahl, E. Ong and Z. Hasan, *Applied Physics Letters*, 1998, **72**, 1308-1310.
12. K. Balamurugan, N. Harish Kumar, B. Ramachandran, M. S. Ramachandra Rao, J. Arout Chelvane and P. N. Santhosh, *Solid State Communications*, 2009, **149**, 884-887.
13. G. W. Dietz, M. Schumacher, R. Waser, S. K. Streiffer, C. Basceri and A. I. Kingon, *Journal of Applied Physics*, 1997, **82**, 2359-2364.
14. P. K. Gallagher, F. Schrey and F. V. DiMarcello, *Journal of the American Ceramic Society*, 1963, **46**, 359-365.
15. S. Komarneni, Q. Li, K. M. Stefansson and R. Roy, *Journal of Materials Research*, 1993, **8**, 3176-3183.
16. R. K. Roeder and E. B. Slamovich, *Journal of the American Ceramic Society*, 1999, **82**, 1665-1675.
17. F. Schrey, *Journal of the American Ceramic Society*, 1965, **48**, 401-405.
18. L. Shaohui, Z. Jiwei, W. Jinwen, X. Shuangxi and Z. Wenqin, *ACS Applied Materials & Interfaces*, 2014, **6**, 1533-1540.
19. S. Suasmoro, S. Pratapa, D. Hartanto, D. Setyoko and U. M. Dani, *Journal of the European Ceramic Society*, 2000, **20**, 309-314.
20. Y. B. Khollam, H. S. Potdar, S. B. Deshpande and A. B. Gaikwad, *Materials Chemistry and Physics*, 2006, **97**, 295-300.
21. P. C. Joshi and M. W. Cole, *Applied Physics Letters*, 2000, **77**, 289-291.
22. S. Yong Cha, Byung-Tak Jang and H. Chul Lee, *Japanese Journal of Applied Physics*, 1999, **38**, L49.
23. S.-Y. Chen, H.-W. Wang and L.-C. Huang, *Japanese Journal of Applied Physics*, 2001, **40**, 4974.
24. K. Hyun Yoon, J. Chan Lee, Jihoon Park, D. Heon Kang, C. Moo Song and Y. Gyo Seo, *Japanese Journal of Applied Physics*, 2001, **40**, 5497.
25. K.-T. Kim and C.-I. Kim, *Microelectronic Engineering*, 2003, **66**, 835-841.
26. P. Pahuja, R.K. Kotnala, R.P. Tandon, *J. Alloys and Compound* 2014,**617**,140-148
27. X. Wang, S. lv, C. Zhang, Q. Hu and L. Li, *Journal of Alloys and Compounds*, 2013, **576**, 262-264.
28. Y. Ye and T. Guo, *Ceramics International*, 2009, **35**, 2761-2765.
29. R. W. Schwartz, *Chemistry of Materials*, 1997, **9**, 2325-2340.
30. L. Xiao, K.-L. Choy and I. Harrison, *Surface and Coatings Technology*, 2011, **205**, 2989-2993.
31. M. Liu, C. Ma, G. Collins, J. Liu, C. Chen, L. Shui, H. Wang, C. Dai, Y. Lin, J. He, J. Jiang, E. I. Meletis and Q. Zhang, *Crystal Growth & Design*, 2010, **10**, 4221-4223.
32. Z. Fu, A. Wu and P. M. Vilarinho, *Chemistry of Materials*, 2006, **18**, 3343-3350.
33. Y. Li and Y. Qu, *Materials Chemistry and Physics*, 2008, **110**, 155-159.
34. J. Liao, X. Wei, Z. Xu, X. Wei and P. Wang, *Materials Chemistry and Physics*, 2012, **135**, 1030-1035.
35. J. Wang, T. Zhang, R. Pan, Z. Ma and J. Wang, *Physica B: Condensed Matter*, 2012, **407**, 160-164.
36. H.-Y. Tian, W.-G. Luo, X.-H. Pu, P.-S. Qiu, X.-Y. He and A.-l. Ding, *Thermochimica Acta*, 2000, **360**, 57-62.
37. D. Yan, Z. Xu, X. Chen, D. Xiao, P. Yu and J. Zhu, *Ceramics International*, 2012, **38**, 2785-2791.
38. R. Z. Hou, A. Wu and P. M. Vilarinho, *Chemistry of Materials*, 2009, **21**, 1214-1220.
39. M. M. Rashad, A. O. Turky and A. T. Kandil, *J Mater Sci: Mater Electron*, 2013, **24**, 3284-3291.
40. C. B. Samantaray, A. Roy, M. Roy, M. L. Mukherjee and S. K. Ray, *Journal of Physics and Chemistry of Solids*, 2002, **63**, 65-69.
41. L. S. Cavalcante, J. C. Sczancoski, F. S. De Vicente, M. T. Frabbro, M. S. Li, J. A. Varela and E. Longo, *J Sol-Gel Sci Technol*, 2009, **49**, 35-46.
42. J. Wang, J. Xiang, S. Duo, W. Li, M. Li and L. Bai, *J Mater Sci: Mater Electron*, 2009, **20**, 319-322.
43. R. Thielsch, K. Kaemmer, B. Holzapfel and L. Schultz, *Thin Solid Films*, 1997, **301**, 203-210.
43. C. B. Samantaray, M. L. Nanda Goswami, D. Bhattacharya, S. K. Ray and H. N. Acharya, *Materials Letters*, 2004, **58**, 2299-2301.
44. X. Wang, M. Gu , B. Yang , S. Zhu , W. Cao, *Microelectronic Engineering*, 2003, **66**,855-859
45. M. B. González, A. Wu and P. M. Vilarinho, *Chemistry of Materials*, 2006, 18, 1737-1744.
46. M. M. Rashad, D. A. Rayan, A. O. Turky and M. M. Hessien, *Journal of Magnetism and Magnetic Materials*, 2015, **374**, 359-366.

TOC

Monodispersed barium strontium titanate $Ba_{0.5}Sr_{0.5}TiO_3$ nanopowders synthesized using oxalate precursor route based on low cost starting materials.